Iterative Adaptive Approach for Respiratory Estimation using SISO, SIMO, and MIMO Radars

Seyedeh Fatemeh Mirhosseini*, Mohammad Alaee-Kerahroodi*, Palak Dave, Andreas Olk**, Udo Schroeder ****

*University of Luxembourg, Luxembourg
email: fatemeh.mirhosseini@uni.lu , mohammad.alaee@uni.lu

**IEE S.A., Luxembourg
email: palak.dave@iee.lu , andreas.olk@iee.lu , udo.schroeder@iee.lu

Abstract: *Radar-based vital sign monitoring has gained attention due to its non-contact and non-invasive nature, offering advantages over traditional methods such as ECG electrodes and camera-based systems. This paper presents the Iterative Adaptive Approach (IAA) for robustly estimating respiration rate using BGT60LTR11AIP, and BGT60TR13C from Infineon and IWR6843ISK from Texas Instruments, which are respectively, SISO, SIMO, and MIMO radar demo boards. By adaptively refining signal processing, through experimental analysis the proposed method steps to mitigate the impact of environmental disturbances and enhance the fidelity of vital sign measurements.*

1. Introduction

The demand for reliable and user-friendly health monitoring systems has increased significantly. Traditional methods, such as electrocardiogram (ECG) electrodes and photoplethysmograph (PPG) sensors [1], although effective, require physical contact with the user and are often intrusive. Camera-based systems [2], although non-contact, rely on visual data, which can be affected by lighting conditions and user positioning, leading to inconsistent results. Radar sensors, in contrast, offer a unique advantage in that they operate independently of light conditions and do not require direct contact, making them an ideal choice for monitoring vital signs in everyday environments.

Radars such as Pulse Doppler and frequency modulated continuous wave (FMCW) systems [3] have shown promise in capturing physiological signals. These radars utilize the received signal phase information to detect subtle chest movements caused by respiration and heartbeat [4, 5]. Despite advancements, radar-based vital sign monitoring faces challenges, including signal interference, noise, motion artifacts, and the complexity of extracting vital signs from raw radar data. Existing approaches often rely on classical signal processing techniques, such as Fourier transform-based spectral analysis, which can be limited by resolution and sensitivity to noise. Parametric methods, which assume specific statistical models for the signal, can improve resolution but are often sensitive to model assumptions and require high computational resources [6].

This research was supported by Luxembourg FNR CORE IF 18856415 - VITALRAD Grant.

To address these challenges, this paper investigates the use of Iterative Adaptive Approach (IAA) for vital sign monitoring using Pulse Doppler and FMCW radars. IAA's foundation lies in solving a Weighted Least Squares (WLS) problem iteratively to estimate signal amplitudes and phase and was introduced in the application of source localization and sensing [7]. The approach has been applied in different signal processing applications, as a few examples are sidelobe suppression and migration correction of migrating targets [8], Multiple-Input Multiple-Output (MIMO) imaging with extrapolation for automotive radars [9], multiple object localization and vital sign monitoring using Ultra-Wideband (IR-Ultra Wideband (UWB)) MIMO radar [10], and vital signs detection with dual-band Continuous Wave (CW) radar [11]. This approach enhances signal fidelity and ensures robust estimation of breathing and heart rates, while mitigating the effects of noise and interference. In this paper, we apply IAA to radar data collected using three distinct hardware platforms: the Infineon BGT60LTR11 Pulse Doppler radar [12] as a Single-Input Single-Output (SISO) system, the Infineon BGT60TR13C radar [13] as a Single-Input Multiple-Output (SIMO) FMCW radar, and the IWR6843ISK radar from Texas Instrument (TI) [14] as a MIMO FMCW radar. These systems provide a diverse set of configurations to evaluate the performance of IAA in vital sign monitoring applications.

The paper is organized as follows. The system model is described in Section 2. The Radar Setup is in Section 3. The measurement results are presented in Section 4. The conclusion is given in Section 5 [1].

2. System Model

Radar-based vital sign monitoring relies on detecting chest movement caused by respiration. The phase shift of the received radar signal, proportional to displacement, is expressed as:

$$\phi_d(t) = \frac{4\pi(d_0 + x(t))}{\lambda}, \tag{1}$$

where d_0 is the initial radar-target distance, $x(t)$ represents chest movement, and $\lambda = \frac{c}{f}$ is the radar wavelength. To extract this phase information with radar, the received radar signal is processed through In-phase (I) and Quadrature (Q) demodulation and then digitized by an analog to digital converter (ADC), as shown in Figure 1a. For the Pulse Doppler radar, the signal undergoes filtering and down-conversion to observe Doppler shifts caused by chest movement, providing a detailed analysis of respiratory patterns. For the FMCW radar, the beat signal is processed using a range-Fast Fourier Transform (FFT) [15], enabling identification of the target's range bin. The slow-time signal, extracted from radar echoes over time and sampled at the pulse repetition frequency (Pulse Repetition Frequency (PRF)), provides slow-time I and Q for vital signs estimation.

In SIMO and MIMO configurations (BGT60TR13C and IWR6843ISK radars), beamforming is employed to direct the radar's sensitivity toward the target location. This enhances the isolation

[1] Notation: $\mathbb{R}^N$ denotes the N-dimensional real vector space. We use bold-face uppercase $\mathbf{X}$ for matrices and bold-face lowercase $\mathbf{x}$ for vectors. $||\cdot||^2$ is norm-2 of a matrix. The transpose operator is denoted by $(\cdot)^T$. The sets of complex numbers, real numbers, and Hermitian operations are denoted by $\mathbb{C}^N$, $\mathbb{R}^N$, $(\cdot)^H$, respectively.

of vital sign signals, particularly respiration, while reducing the impact of environmental interference. After beamforming, the discrete signal at the range bin of interest can be modeled as (for BGT60LTR11AIP this would be the signal after filter and direct digital synthesizer (DDS) block as illustrated in Figure 1a):

$$y[n] = I[n] + jQ[n] + W[n], \tag{2}$$

where $W[n] = W_0[n] + \sum_{i=1} W_i[n]$. Here, $W_0[n]$ represents independent and identically distributed (IID) Gaussian noise, while $W_i[n]$ accounts for environmental noise observed during in-lab measurements. To ensure accuracy, I and Q imbalance compensation are applied as described in [16]. For breathing rate estimation using BGT60LTR11AIP, BGT60TR13C and IWR6843ISK radars, the angle of the complex-valued signal $y[n]$, derived from the radar echoes, is first unwrapped to mitigate phase discontinuities. The unwrapped phase is then filtered within the predefined breathing rate frequency band of $[0.2, 0.65]$ Hz. This filtering isolates the respiratory components of the signal. Subsequently, IAA is applied to accurately estimate the breathing rate at each time interval. The experimental setup is depicted in Figure 1b, which also illustrates the laboratory environment for data collection. To validate the radar-based breathing rate measurements, the NeuLog Respiration Monitor Belt [17] was utilized as the ground truth device.

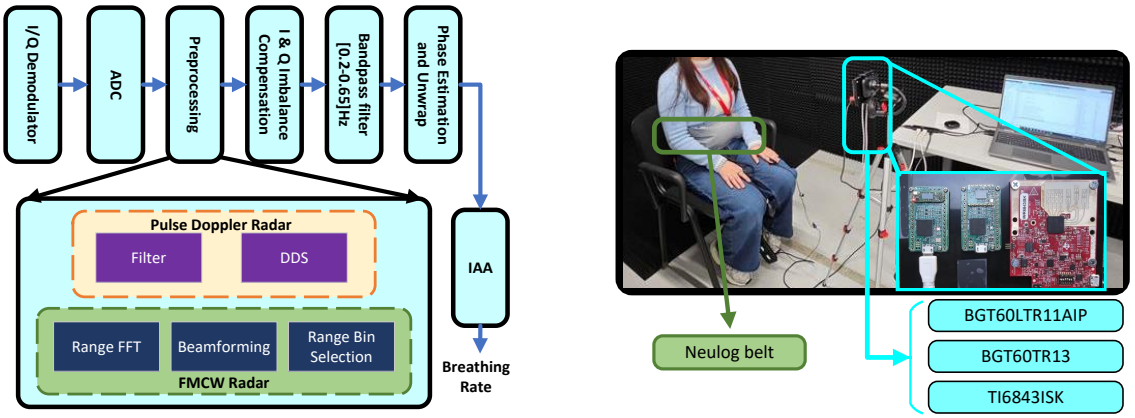

(a) (b)

Figure 1: (a) Block diagram for human breathing rate estimation using IAA (b) Laboratory environment for breathing rate estimation using all three radars.

2.1. Iterative Adaptive Approach Based on Weighted Least Square

Let us assume $\tilde{\phi}[n]$ is the filtered unwrapped phase of the received signal at discrete time of n; i.e., slow-time signal for BGT60TR13C and IWR6843ISK, and a downsampled signal for BGT60LTR11AIP. So, $\tilde{\boldsymbol{\phi}}_M = [\tilde{\phi}[1], \ldots, \tilde{\phi}[M]]^T \in \mathbb{R}^M$ is the entire sequence of one snapshot from the filtered unwrap phase, where M is the total number of incidents. Finding out the most powerful peaks in the frequency domain based on IAA method [10, 18], Let us assume that the phase vector, $\tilde{\boldsymbol{\phi}}_M$, has M samples. Let $\mathbf{a}_M(\omega) = [1, e^{j\omega}, \ldots, e^{j(M-1)\omega}]^T \in \mathbb{C}^M$

denote the steering vector where $\omega \in [0, 2\pi)$ represents the frequency. A uniform frequency grid with N grid points can be considered as $\omega_n = \frac{2\pi n}{N},\ n = 0, 1, \ldots, N-1$ and $\mathbf{A}_M = [\mathbf{a}_M(\omega_0), \mathbf{a}_M(\omega_1), \ldots, \mathbf{a}_M(\omega_{N-1})] \in \mathbb{C}^{M \times N}$. So, the received unwrapped phase signal can be modeled as $\tilde{\boldsymbol{\phi}}_M = \mathbf{A}_M \mathbf{x}_N + \mathbf{e}_M$, where $\mathbf{x}_N = [x_0, x_1, \ldots, x_{N-1}]^T \in \mathbb{C}^N$, with x_n denoting the amplitude with complex value corresponding to ω_n and $\mathbf{e}_M$ denoting the noise part. Given $\tilde{\boldsymbol{\phi}}_M$ and $\mathbf{A}_M$, IAA is minimizing the following weighted least square cost function,

$$||\tilde{\boldsymbol{\phi}}_M - \mathbf{a}_M(\omega_n) x_n||^2_{\mathbf{Q}_M^{-1}(\omega_n)},\ n = 0, 1, \ldots, N-1, \tag{3}$$

where $||\boldsymbol{\zeta}||^2_{\mathbf{Q}_M^{-1}(\omega_n)} = \boldsymbol{\zeta}^H \mathbf{Q}_M^{-1}(\omega_n) \boldsymbol{\zeta}$, and $\mathbf{Q}_M(\omega_n) = \mathbf{R}_M - p_n \mathbf{a}_M(\omega_n) \mathbf{a}_M^H(\omega_n)$, is the IAA interference (other signals at the frequency grid points in addition to ω_n) and the noise covariance matrix. $p_n = |x_n|^2$ is considered as the signal power at grid point ω_n. Moreover, the IAA covariance matrix has the expression $\mathbf{R}_M = \mathbf{A}_M \mathbf{P}_N \mathbf{A}_M^H$, where $\mathbf{P}_N$ is a diagonal matrix with diagonal entries from the vector $\mathbf{p}_N = [p_0, p_1, \ldots, p_{N-1}]^T$ denoting the signal power corresponding to the frequency which is ω_n. Minimizing equation (3) considering x_n, $n = 0, 1, \ldots, N-1$ is as

$$x_{IAA}(n) = \frac{\mathbf{a}_M^H(\omega_n) \mathbf{Q}_M^{-1}(\omega_n) \tilde{\boldsymbol{\phi}}_M}{\mathbf{a}_M^H(\omega_n) \mathbf{Q}_M^{-1}(\omega_n) \mathbf{a}_M(\omega_n)},\ n = 0, 1, \ldots, N-1. \tag{4}$$

3. Spectrum of transmitted signal

Table 1 presents the principle characteristics of three radar modules used in this paper: Infineon BGT60LTR11AIP, Infineon BGT60TR13C, and Texas Instruments IWR6843ISK. The table shows the available frequency range of operation based on the datasheet, the maximum number of receive (Rx) antennas, the maximum number of transmit (Tx) antennas, and the type of radars and manufacturers. BGT60LTR11AIP, is a pulse radar used for motion detection. Based on the feasible frequency range of this radar as mentioned in Table 1, the frequency is set to 61.04 GHz. Moreover, the pulse repetition frequency is set to 4000 Hz, while the down conversion rate is 200 samples, therefore, the vital sign sampling frequency for this radar is 20 Hz. BGT60TR13C, is a SIMO FMCW radar. The operating frequency range is $58.0 - 63.5$ GHz for this radar. Azimuth and elevation field of view for this sensor is $90°$. It has 3 Rx and 1 Tx antennas. In this research, the sampling rate for this radar was set to 20 Hz. IWR6843ISK is also a MIMO FMCW radar from Texas Instruments operating in the range of 60 GHz to 64 GHz. This mmWave radar contains 4 Rx and 3 Rx antennas with $120°$ azimuth field of view and $30°$ elevation field of view. The sampling rate of this radar is also set to 20 Hz.

Table 1: Comparison of Radar Characteristics

Radar system	**BGT60LTR11AIP [12]**	**BGT60TR13C [13]**	**IWR6843ISK [14]**
Frequency Range	61 GHz-61.5 GHz	58 GHz-63.5 GHz	60 GHz-64 GHz
Number of Antennas (max)	Rx = 1, Tx = 1	Rx = 3, Tx = 1	Rx = 4, Tx = 3
Radar type	Pulse Radar	SIMO FMCW	MIMO FMCW
Manufacturer	Infineon	Infineon	Texas Instruments

Measurement setup As a first step in this work, we performed an analysis of the transmitted signal of the three radar sensors in terms of spectrum parameters. The experimental setup for spectrum analysis is depicted in Figure 2. The transmitted radar signals are captured by a horn antenna (Mi-Wave 261V 25/385 [19]), which features 25 dBi gain and operates in the V-band, i.e., 50 - 75 GHz. The captured signal is then passed to the downconversion stage. In the downconversion stage, the FS-Z75 mixer [20] is employed. The mixer converts the high-frequency radar signal to an intermediate frequency (IF). The MXG N5183B signal generator provides the required local oscillator [21]. The local oscillator frequency used during the measurements here is 9.95 GHz in the case of the Infineon CW and TI FMCW radar, and it is 9.56 GHz in the case of Infineon FMCW radar . The downconverted signal is in the range of approximately DC - 6 GHz depending on the LO and it is directed to the FSV3030 ROHDE & SCHWARZ spectrum analyzer [22]. The entire system is calibrated using a vector network analyzer (VNA) and a second horn antenna as reference source.

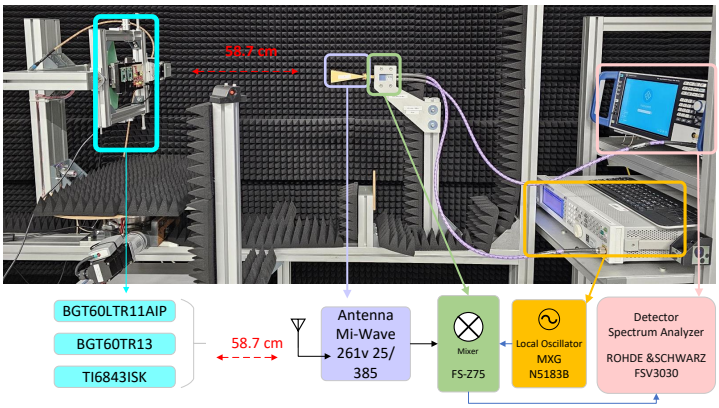

Figure 2: Experimental setup for the characterization of the radiated signal of the radar systems

Results The spectrum of the transmitted radar signal is expressed in terms of effective isotropically radiated power P_{EIRP}. This includes the conducted power of the radar chip, properties of the Tx antenna and path losses in the feeding lines. The spectrum for the three radars is shown in Figure 3. The radiated power P_{EIRP} ranges from 5.82 dBm to 8.99 dBm for the BGT60TR13C (Infineon FMCW) radar which is fairly consistent, and from 7.72 dBm to 13.67 dBm for the IWR6843ISK (TI FMCW) radar, which is a larger variation. Non-ideal matching of the antennas to the chip, reflection losses in the feeding network or a less stable Radio Frequency (RF) source in the chip can be the reasons for this large variation in the latter radar. The radiation of all Tx channels contributes to the result of the acquired signal since the sweep time is 10 seconds, which is sufficiently long in proportion to the time. We note that the variation in the noise floor is due to the artifact of the measurement system. The noise floor of the spectrum analyzer is generally almost constant, but since it is combined with a passive mixer, the noise floor is affected by the mixer conversion loss and LO settings. However, in all cases, the noise floor is low enough to make the transmitted radar signal discernible, i.e., less than 3 dBm below the weakest features of the radar signal. More dynamic range can be achieved using active mixers instead.

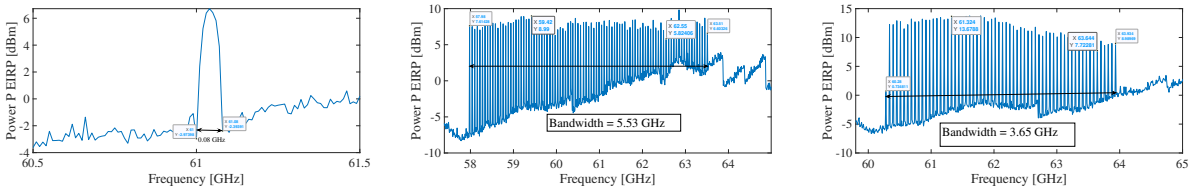

(a) (b) (c)

Figure 3: The spectrum of the radiated radar signal in terms of effective isotropically radiated power P_{EIRP} for the three radar systems (a) BGT60LTR11AIP (b) BGT60TR13C (c) and IWR6843ISK.

4. Measurement

The radars are kept at a 75 cm distance from the user for the experimental breathing rate measurement within the laboratory. The sampling frequency of the radars is 20 Hz, and for the Neulog belt (benchmark) it is considered 10 Hz. Using the IAA method for spectral estimation, it accurately estimates the breathing rate as shown in Figure 4. The amount of Root Mean Square Error (RMSE) is computed as $E = \sqrt{\frac{1}{n}\sum_{i=1}^{n}|A_i - F_i|^2}$, where n is the total length of the signal, A_i is each element of the ground-truth signal captured from the Neulog belt in time, and F_i is the signal captured from the radars. The amount of root mean square error for these three radars is equal to 1.59 bpm for Pulse Doppler radar (BGT60LTR11AIP), 1.43 bpm for SIMO FMCW radar (BGT60TR13C) and 1.42 bpm for TI FMCW radar (IWR6843ISK). As a result, the radar mentioned last has the best accuracy compared to the other two radars. In addition, Figure 5 indicates RMSE for four participants measured under laboratory conditions. Based on that, IWR6843ISK and BGT60TR13C as a FMCW radar perform the best compared to BGT60LTR11AIP.

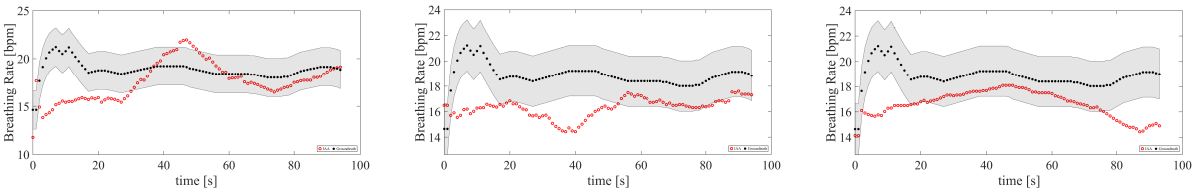

(a) (b) (c)

Figure 4: The comparison of the estimated breathing signal using IAA with the ground-truth signal for (a) BGT60LTR11AIP (b) BGT60TR13C and (c) IWR6843ISK.

5. Conclusion

In this paper, we characterize three different mm-wave radar sensors (BGT60LTR11AIP, BGT60TR13C and IWR6843ISK) using horn antennas, down-converter and spectrum analyzer. To estimate the breathing rate of the participants in a controlled laboratory environment,

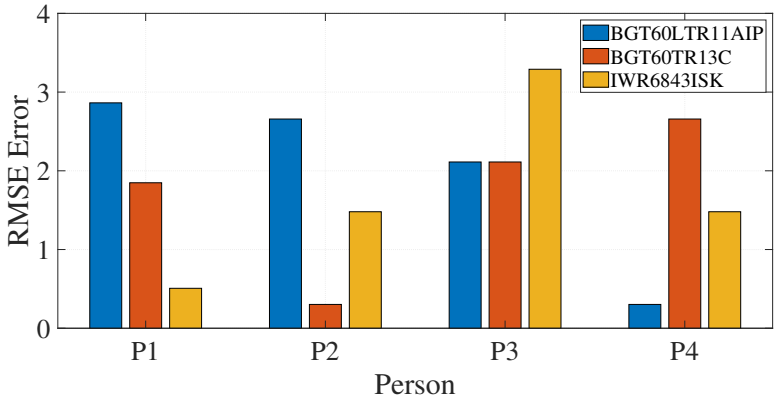

Figure 5: Root mean square error for 4 participants sitting still in the laboratory condition, measured with three types of radars.

we used the IAA technique. We compared the radar-based breathing rate estimates with the ground-truth signal captured from the Neulog sensor. The results showed that radar sensors, when combined with the IAA algorithm, could successfully estimate the breathing rate with high accuracy, demonstrating their potential for non-invasive biometric monitoring in health-related applications. Moreover, although it is expected that the radar with the maximum bandwidth will perform the best, among the radars mentioned, IWR6843ISK and BGT60TR13C which are FMCW radars perform the better compared to BGT60LTR11AIP.

References

[1] B.-G. Lee and W.-Y. Chung, "Driver alertness monitoring using fusion of facial features and bio-signals," *IEEE Sensors Journal*, vol. 12, no. 7, pp. 2416–2422, 2012.

[2] L. Leicht, M. Walter, M. Mathissen, C. H. Antink, D. Teichmann, and S. Leonhardt, "Unobtrusive measurement of physiological features under simulated and real driving conditions," *IEEE Transactions on Intelligent Transportation Systems*, vol. 23, no. 5, pp. 4767–4777, 2022.

[3] L. Anitori, A. de Jong, and F. Nennie, "Fmcw radar for life-sign detection," in *2009 IEEE Radar Conference*. IEEE, 2009, pp. 1–6.

[4] W. Hu, Z. Zhao, Y. Wang, H. Zhang, and F. Lin, "Noncontact accurate measurement of cardiopulmonary activity using a compact quadrature doppler radar sensor," *IEEE Transactions on Biomedical Engineering*, vol. 61, no. 3, pp. 725–735, 2014.

[5] B. Elmakhzangy, F. Aziz, Y. ElZawahry, C. Maufroy, U. Schneider, and M. F. Huber, "Improved multi-person vital signs estimation algorithm in sitting and standing positions using mimo fmcw radar," in *2023 IEEE International Radar Conference (RADAR)*, 2023, pp. 1–6.

[6] P. Stoica, R. L. Moses *et al.*, *Spectral analysis of signals*. Pearson Prentice Hall Upper Saddle River, NJ, 2005, vol. 452.

[7] T. Yardibi, J. Li, P. Stoica, M. Xue, and A. B. Baggeroer, "Source localization and sensing: A Nonparametric Iterative Adaptive Approach Based on Weighted Least Squares," *IEEE Transactions on Aerospace and Electronic Systems*, vol. 46, no. 1, pp. 425–443, 2010.

[8] J. Tian, B. Zhang, W. Cui, and S. Wu, "Joint Iterative Adaptive Approach for sidelobe suppression and migration correction of migrating targets," *IEEE Transactions on Aerospace and Electronic Systems*, pp. 1–23, 2024.

[9] B.-s. Kim, J. Lee, S. Kim, and R. M. Narayanan, "MIMO imaging method with extrapolation-iterative adaptive approach-based super-resolution technique for automotive radar," in *2024 IEEE Radar Conference (RadarConf24)*, 2024, pp. 1–6.

[10] X. Shang, J. Liu, and J. Li, "Multiple object localization and vital sign monitoring using IR-UWB MIMO radar," *IEEE Transactions on Aerospace and Electronic Systems*, vol. 56, no. 6, pp. 4437–4450, 2020.

[11] C. Huan, P. Kontou, S. B. Smida, and D. E. Anagnostou, "Dual-band CW radar system for vital signs detection with interference cancellation method," *IEEE Transactions on Microwave Theory and Techniques*, pp. 1–16, 2024.

[12] Infineon Technologies AG. (2024) Demo BGT60LTR11AIP getting started with the XENSIV™ 60GHz BGT60LTR11AIP radar sensor demo board for motion sensing. [Online]. Available: https://www.infineon.com/cms/en/product/evaluation-boards/demo-bgt60ltr11aip/

[13] I. T. AG. (2024) DEMO BGT60TR13C: Getting started with the XENSIV™ 60GHz BGT60TR13C radar sensor demo board for advanced sensing. [Online]. Available: https://www.infineon.com/cms/en/product/evaluation-boards/demo-bgt60tr13c/

[14] T. Instruments. (2024) IWR6843 evaluation module for single-chip 60GHz long-range antenna mmwave sensor. [Online]. Available: https://www.ti.com/product/IWR6843ISK/part-details/IWR6843ISK

[15] R. Amar, M. Alaee-Kerahroodi, P. Babu, and B. S. M. R., "Designing interference-immune doppler-tolerant waveforms for radar systems," *IEEE Transactions on Aerospace and Electronic Systems*, vol. 59, no. 3, pp. 2402–2421, 2023.

[16] J. J. de Witt and G.-J. van Rooyen, "A blind I/Q imbalance compensation technique for direct-conversion digital radio transceivers," *IEEE Transactions on Vehicular Technology*, vol. 58, no. 4, pp. 2077–2082, 2009.

[17] Neulog. (2011-2017) Neulog. [Online]. Available: https://neulog.com/respiration-monitor-belt/

[18] M. Xue, L. Xu, and J. Li, "IAA spectral estimation: Fast implementation using the Gohberg–Semencul factorization," *IEEE Transactions on Signal Processing*, vol. 59, no. 7, pp. 3251–3261, 2011.

[19] "Mi-Wave's 261," https://system.miwv.com/storage/datasheets/261V-25-385.pdf?v=1629231541, accessed: 2010-09-30.

[20] RPG Radiometer physics GmbH. (2014) Fs-z75. [Online]. Available: https://www.rohde-schwarz.com/nl/products/test-and-measurement/harmonic-mixers/rpg-fs-zxx-harmonic-mixers_63493-421184.html

[21] Keysight. (2024) Demo N5183x Keysight N5183x MXG X-Series microwave analog signal generator. [Online]. Available: https://www.keysight.com/us/en/product/N5183B/mxg-x-series-microwave-analog-signal-generator-9-khz-40-ghz.html

[22] Rohde and Schwarz. (2024) The rohde & schwarz signal and spectrum analyzer portfolio. [Online]. Available: https://www.rohde-schwarz.com/products/test-and-measurement/signal-and-spectrum-analyzers_63665.html?mid=10918&midx=r-eu-brand-spectrum-analyzer_r-eu-brand_search_text-ad_r-eu_&kw=r%26s%20fsv